AIP | Journal of Applied Physics

Determination of optical and microstructural parameters of ceria films

Tae-Sik Oh, Yury S. Tokpanov, Yong Hao, WooChul Jung, and Sossina M. Haile

Citation: J. Appl. Phys. **112**, 103535 (2012); doi: 10.1063/1.4766928
View online: http://dx.doi.org/10.1063/1.4766928
View Table of Contents: http://jap.aip.org/resource/1/JAPIAU/v112/i10
Published by the American Institute of Physics.

Determination of optical and microstructural parameters of ceria films

Tae-Sik Oh,[1,a)] Yury S. Tokpanov,[2] Yong Hao,[1,b)] WooChul Jung,[1] and Sossina M. Haile[1]
[1]*Materials Science, California Institute of Technology, Pasadena, California 91125, USA*
[2]*Moscow Institute of Physics and Technology, Moscow, Russia*

(Received 30 March 2012; accepted 24 October 2012; published online 30 November 2012)

Light-matter interactions are of tremendous importance in a wide range of fields from solar energy conversion to photonics. Here the optical dispersion behavior of undoped and 20 mol. % Sm doped ceria thin films, both dense and porous, were evaluated by UV-Vis optical transmission measurements, with the objective of determining both intrinsic and microstructural properties of the films. Films, ranging from 14 to 2300 nm in thickness, were grown on single crystal YSZ(100) and MgO(100) using pulsed laser deposition (both dense and porous films) and chemical vapor deposition (porous films only). The transmittance spectra were analyzed using an in-house developed methodology combining full spectrum fitting and envelope treatment. The index of refraction of ceria was found to fall between 2.65 at a wavelength of 400 nm and 2.25 at 800 nm, typical of literature values, and was relatively unchanged by doping. Reliable determination of film thickness, porosity, and roughness was possible for films with thickness ranging from 500 to 2500 nm. Physically meaningful microstructural parameters were extracted even for films so thin as to show no interference fringes at all. © *2012 American Institute of Physics*.
[http://dx.doi.org/10.1063/1.4766928]

I. INTRODUCTION

Light-matter interactions are of tremendous importance in a wide range of fields from solar energy conversion to photonics. The complex refractive index $[\boldsymbol{n}(\lambda) = n(\lambda) - ik(\lambda)]$ is the fundamental optical constant that governs these interactions and its accurate determination is of prime importance. In any optical measurement, the response from the sample depends not only on its inherent optical properties but also on its microstructure. Thus, optical transmittance through a thin film depends on features such as thickness, roughness, and porosity in addition to $\boldsymbol{n}$. This interdependence conversely implies that, with a knowledge of the complex refractive index, transmittance measurements can be employed to determine the microstructural characteristics. Amongst available tools for film microstructural characterization, the UV-VIS transmittance method is particularly attractive because it is quick and non-destructive and can probe a large area of sample. It can also be used for relatively thick films that are unsuitable for x-ray based techniques such as x-ray reflectivity (XRR) or Laue oscillation.

The essence of a transmission measurement is simply to determine the fraction of light that is transmitted through the sample of interest over a given wavelength range. Transmission through a film on a substrate deviates from 1 not only because of absorption (non-zero imaginary component of the complex index) but also because reflection at interfaces creates interference fringes. Analysis by the widely used envelope method[1] of the maximal and minimal transmittance values associated with these fringes and the wavelength separation between them enables one to determine both $\boldsymbol{n}(\lambda)$ and thickness. However, as the thickness of the film decreases, the number of interference fringes in a given wavelength range decreases, increasing the uncertainty in the derived parameters, and the method becomes inapplicable.

In this work, we explore the properties of ceria films that can be extracted from transmittance measurements using a combination of data analysis approaches. For compositions for which the index of refraction is first fully characterized using dense, smooth, thick films, we show that it is possible to accurately obtain film thickness and porosity from films with arbitrary features. The optical properties of undoped and Sm-doped ceria measured and reported here are interpreted in terms of the electronic band structure. The microstructural properties of films obtained from different deposition techniques are discussed in terms of the film growth characteristics.

II. EXPERIMENTAL METHODS

A. Sample preparation

Ceria films were grown by both pulsed laser deposition (PLD) and chemical vapor deposition (CVD). PLD was carried out using a Neocera deposition system equipped with a coherent 102 KrF 248 nm excimer laser, operated at a power density of about 2 J/cm^2 and deposition frequency of 20 Hz. Targets of either undoped or 20 mol. % Sm doped ($Sm_{0.2}Ce_{0.8}O_{1.9-\delta}$ or 20SDC) were fabricated in-house using commercial powders (undoped: Sigma Aldrich 202975, 99.995% pure; 20% doped: Fuel Cell Materials, 20SDC-HP, trace metal impurity ~160 ppm wt.). To minimize the influence of the limited size of the laser plume on the uniformity of the films, the substrates were arranged at the center of the sample stage and rotated at a constant angular speed. The

[a)]Present address: Department of Chemical and Biomolecular Engineering, University of Pennsylvania, Philadelphia, Pennsylvania 19014-6315, USA.
[b)]Present address: Laboratory of Energy Systems and Renewable Energy Institute of Engineering Thermophysics, Chinese Academy of Sciences 11 Beisihuanxi Rd, Beijing, 100190, People's Republic of China.

substrate was maintained a temperature of 600–650 °C during deposition, and a cooling rate of 10 °C/min was used prevent the films from cracking due to thermal expansion mismatch. Porosity in the deposited ceria film was varied by varying the background pressure of oxygen (5 mTorr for dense films, 100 mTorr for porous films[2]). Regardless of eventual film porosity, typical PLD growth rate was 20 nm min^{-1}. Film growth by CVD was carried out using an in-house constructed vertical cold-wall reactor, and compositions were limited to undoped ceria. The cerium precursor, $Ce(tmhd)_4$ (Strem, CAS: 18960-54-8, 99.9% cation purity), was used without further purification. The precursor was evaporated at a temperature of 190 °C. The total system pressure during deposition was varied within a range of 1–3 Torr and the substrate temperature held at between 450 and 500 °C. The oxygen to argon flow ratio was kept at 1:2. The typical deposition rate was 15 to 20 nm min^{-1}.

Films were grown on 8 mol. % Y_2O_3-doped ZrO_2 [YSZ(100)] and MgO(100) single-crystal substrates (MTI Corporation), polished on both sides and with dimensions 1 cm × 1 cm × 0.5 mm. The root mean square (rms) surface roughness of the as-received substrates, as measured in-house by atomic force microscopy (AFM), was below 0.5 nm and the peak-to-valley roughness below 3.5 nm. It is noted that $n_{YSZ} > n_{ceria} > n_{MgO}$ and thus this choice of substrates enables assessment of the applicability of the optical analysis methods to arbitrary substrate-film combinations.

B. Measurements

Optical transmittance was measured using an Ocean optics HR2000CG-UV-NIR high-resolution, miniature, fiber-optic spectrometer, with a data collection range of 200 to 800 nm (beyond 800 nm the data were too noisy to be useful) and a 0.47 nm data point interval. The raw spectra for the wavelength range 400 to 800 nm were each converted to 500 equally spaced data points for analysis. No smoothing of any sort was applied. In all cases, when the sample was physically inverted such that the incident photons interacted with substrate first, there was essentially no change in transmittance trace. Transmittance spectra from blank substrates were also measured over the same wavelength range in order to obtain the substrate index of refraction as required for the analysis.

AFM roughness measurements were performed using a Park Systems XE-70 in non-contact mode. Occasional large particulates that formed on the PLD surface were avoided for the roughness measurement. These particulates were found to have negligible impact on measured transmittance spectra. Plane leveling and subsequent rms roughness estimation were carried out using the GWYDDION 2.25 software package. Film morphology was observed using a ZEISS 1550VP field emission scanning electron microscope (SEM). Examination of fractured cross-sections of films provided an external and independent measure of film thickness. X-ray reflection curves to probe film roughness and density were collected using a Rigaku Smartlab diffractometer with 0.01° steps in two-theta up to 5° and data analyzed using the X'Pert Reflectivity software package. X-ray rocking curves were collected using an X'pert pro MRD system from Panalytical. A scanning white light interferometer (SWLI), Zygo NewView 600, was used to obtain surface topography maps for very thin films (<50 nm). The field of view was 140 μm × 105 μm for all cases.

III. ANALYTICAL METHODS

Analytical expressions for the optical transmission through a system comprised of a thin film exposed to air and deposited on a substrate with zero absorption (i.e., a transparent substrate) and a transmittance of no less than ~0.5 have been derived in the literature. In the wavelength range of interest (400 to 800 nm) MgO and YSZ have negligible extinction coefficient, k, and these expressions are applicable. We consider first the case of an ideally flat, smooth and dense film on a substrate of (arbitrary) finite thickness with the following characteristics:

$$\boldsymbol{n}_{\text{susbtrate}} = s - \mathrm{i}k_s = s(\lambda),$$
$$\boldsymbol{n}_{\text{film}} = n - \mathrm{i}k = n(\lambda) - \mathrm{i}k(\lambda),$$
$$d = \text{film thickness}.$$

The wave-length dependent transmittance, T, for this system is[1,3]

$$T = \frac{Fx}{G - Hx + Kx^2}, \tag{1}$$

where

$$x = \exp(-\alpha d), \tag{1a}$$

$$\alpha = \text{absorption coefficient} = 4\pi k/\lambda, \tag{1b}$$

$$F = 16s(n^2 + k^2), \tag{1c}$$

$$G = [(n+1)^2 + k^2][(n+1)(n+s^2) + k^2], \tag{1d}$$

$$H = [(n^2 - 1 + k^2)(n^2 - s^2 + k^2) - 2k^2(s^2 + 1)] \cdot 2\cos\phi - k[2(n^2 - s^2 + k^2) + (s^2 + 1)(n^2 - 1 + k^2)] \cdot 2\sin\phi, \tag{1e}$$

$$K = [(n-1)^2 + k^2][(n-1)(n-s^2) + k^2], \tag{1f}$$

and

$$\varphi = \text{the phase (in wavelength space) of the interference fringes} = 4\pi nd/\lambda. \tag{1g}$$

Expression (1) describes an oscillating spectrum overlain on a transmittance that shows an overall increase with λ, where the spacing between maxima and minima is given by φ. The value of T at any given wavelength thus depends on three parameters, the real component of the index at that wavelength, the imaginary component (at that wavelength), and the film thickness; accordingly, the problem, at a single wavelength, is underdetermined. Swanepoel circumvented this challenge by introducing the envelope method. The approach treats the overall characteristics of the transmittance function, rather than transmittance values at individual wavelengths, and takes advantage of the fact that the difference in transmittance at maxima and minima, interpolated to

a given wavelength, depends only on n (and is independent of both d and k). The transmittance values at the maxima define the upper envelope, T_U, and those at the minima, the lower envelope, T_L. Because T_U and T_L can be interpolated to arbitrary values of λ, the envelope method allows the index of refraction to be directly computed at any given λ, so long as $T_U(\lambda)$ and $T_L(\lambda)$ are appropriately established. With $n(\lambda)$ known, the spacing between maxima and minima is then used to compute d. Finally, the extinction coefficient is determined after evaluating the absorbance from the separate expression[4]

$$x = \{P + [P^2 + 2QT_\alpha(1 - R_2R_3)]^{1/2}\}/Q, \tag{2}$$

$$R_1 = [(1-n)/(1+n)]^2, \tag{2a}$$

$$R_2 = [(n-s)/(n+s)]^2, \tag{2b}$$

$$R_3 = [(s-1)/(s+1)]^2, \tag{2c}$$

$$P = (R_1 - 1)(R_2 - 1)(R_3 - 1), \tag{2d}$$

$$Q = 2T_\alpha(R_1R_2 + R_1R_3 - 2R_1R_2R_3), \tag{2e}$$

$$T_\alpha = \sqrt{T_U T_L}. \tag{2f}$$

The ultimate effectiveness relies on accurate positioning of the envelope values and identification of the order number of each interference fringe.

Alternatively, if one has knowledge of the functional forms of $n(\lambda)$ and $k(\lambda)$, then one could adjust the parameters of those functions so as to fit a spectrum, calculated according to Eq. (1), to the measured spectrum. Such an approach would utilize the full set $\{T_i\}$ to determine a limited set of parameters, eliminating the situation of an underdetermined problem. The behavior of $n(\lambda)$ for transparent materials has been treated and is discussed in greater detail below. The behavior of $k(\lambda)$ can ideally be obtained from $n(\lambda)$ utilizing the Kramers-Kronig relation. Because the wavelength range of the measurement is finite, however, the treatment is not entirely straightforward. Bhattacharya *et al.* applied such an envelope-free approach to the study of films of $Zn_{1-x}Mg_xO$ with good success, but could do so only upon dividing the spectra into arbitrary regions.[5]

In the present work, we employed a strategy that combines aspects of full spectrum fitting and envelope treatment and is free of arbitrary definitions of absorption regions. The index of refraction, $n(\lambda)$, is assumed to behave according to the Sellmeier equation,

$$\frac{1}{n^2 - 1} = -\frac{A}{\lambda^2} + B, \tag{3}$$

an expression that has been found to accurately represent the behaviors of a large number of transparent materials.[6] As the dispersion characteristics arise from the interaction of light with the bonding electrons, the A and B constants suitably parameterize the behavior for subsequent analysis, as described in detail below. For those measurements in which the objective is to determine optical properties rather than microstructural features, starting estimates of A and B are employed to provide initial estimates of n through Eq. (3) and of k through Eq. (2), where the latter relies on determination of the envelope values $T_U(\lambda)$ and $T_L(\lambda)$. Full spectrum fitting is performed by computing and minimizing the error, χ^2, defined as

$$\chi^2 = \sum_1^N \frac{1}{{\sigma_i}^2}(T_i^{calc} - T_i^{meas})^2, \tag{4}$$

where T is that given in Eq. (1), N is the number of points in the calculation (= 500), and σ_i is the experimental uncertainty in each transmittance point. The latter is taken to be 0.01 over the entire wavelength range of interest based on the transmittance measured from an empty cell ($T = 1$). The analysis is limited to the wavelength regime in which $T \geq 0.5$, corresponding to $\lambda \geq 400$ nm. For the types of films discussed to this point (smooth, dense, and flat), refined parameters are the material properties, A and B. Refinement of the thickness, d, can also be introduced at this stage.

We now consider two microstructural modifications—roughness and porosity—of relevance to films obtained under typical experimental growth conditions. As recognized by Swanepoel,[7] roughness on the film surface has the effect of "softening" the interference fringes in the transmittance spectrum such that T_U and T_L approach each other, but without modification to the wavelength dependence of the position of the extrema. Treatment of the problem requires a physical model of the manner in which the thickness varies. Here, each film is considered to display a mean thickness and a Gaussian distribution of thicknesses about this mean. Numerical implementation is achieved by dividing the film into 5000 equal-footprint vertical columns with heights reflecting the Gaussian distribution. The transmittance is then computed assuming a spatial average over the transmittances through each column, T_j, given by

$$T = \frac{1}{5000}\sum_{j=1}^{5000} T_j(d_j), \tag{5}$$

where the 5000 d_j values are distributed about d with standard deviation r. This standard deviation corresponds to the root-mean-square roughness and ideally matches the value measured directly by AFM.

Porosity in the film has the effect of lowering the effective index of refraction by rendering it an average, in some way, of the bulk properties of the film material (>1) and of air (~1). Following the general approach of effective medium theory, here, the microstructure-specific optical properties of the porous material or two-phase composite (of the solid and air) are replaced with those of a hypothetical dense film with equivalent properties. Available models for the optical properties are developed for the dielectric function, $\boldsymbol{\varepsilon} = \varepsilon_1 - i\varepsilon_2$, which can be mapped to the refractive index according to

$$n = \left(\frac{(\varepsilon_1^2 + \varepsilon_2^2)^{1/2} + \varepsilon_1}{2}\right)^{1/2},$$

$$k = \left(\frac{(\varepsilon_1^2 + \varepsilon_2^2)^{1/2} - \varepsilon_1}{2}\right)^{1/2}. \tag{6}$$

We consider three specific forms of effective medium theory. The first is the symmetric Bruggeman (S-BG) model

for binary mixtures, in which there is no distinction between continuous (matrix) and discontinuous (inclusion) phases; each inclusion is in contact with other inclusions of either phase. The result for sphere-shaped inclusions is expressed as[8]

$$f_b \frac{\varepsilon_b - \varepsilon_{eff}}{\varepsilon_{eff} + \frac{1}{3}(\varepsilon_b - \varepsilon_{eff})} + f_p \frac{\varepsilon_p - \varepsilon_{eff}}{\varepsilon_{eff} + \frac{1}{3}(\varepsilon_p - \varepsilon_{eff})} = 0, \quad (7)$$

where f_b is the volume fraction of oxide; f_p is the volume fraction of pore (total porosity) (fitting parameter, $0 \le f_p \le 0.6$); ε_b is the dielectric function of fully dense oxide; $\varepsilon_p = 1$ (air) $= \varepsilon_p$; and ε_{eff} is the effective dielectric function (oxide/air composite).

Of the two roots to Eq. (7), only one is physically meaningful, and it reads

$$\varepsilon_{eff} = \frac{(3f_b\varepsilon_b - \varepsilon_b - \varepsilon_p + 3f_p\varepsilon_p) + \sqrt{(3f_b\varepsilon_b - \varepsilon_b - \varepsilon_p + 3f_p\varepsilon_p)^2 + 8\varepsilon_b\varepsilon_p}}{4}. \quad (8)$$

The second formalism is the asymmetric Bruggeman (A-BG) model, in which it is assumed that the inclusions, air-filled pores in our case, are always spherical and are coated with matrix material such that they cannot touch one another.[9] The A-BG model yields an implicit form for ε_{eff} as shown below,

$$\frac{\varepsilon_p - \varepsilon_{eff}}{\varepsilon_p - \varepsilon_b} = (1 - f_p)\left(\frac{\varepsilon_{eff}}{\varepsilon_b}\right)^{1/3}. \quad (9)$$

The solution for ε_{eff} from the above is obtained using Sihvola's series expansion method. The complete form can be found in Ref. 10.

Looyenga and Landau-Lifshitz independently derived a third dielectric mixing law (henceforth the LLL model) in which the host and matrix phases are assigned dielectric constant values of $\varepsilon_{eff} + \Delta\varepsilon$ and $\varepsilon_{eff} - \Delta\varepsilon$,[11,12] and no assumptions are made regarding phase distributions. The result is given as

$$\varepsilon_{eff} = [(\varepsilon_p{}^{1/3} - \varepsilon_b{}^{1/3})f_p + \varepsilon_b{}^{1/3}]^3. \quad (10)$$

While there are some instances in which this expression fits experimental data more closely than the Bruggeman expressions [e.g., Ref. 13] and the absence of microstructual assumptions renders the approach attractive, the LLL model fails when the permittivity of the host material differs greatly from that of the inclusion.

It is of value to explore the sensitivity of predicted behavior of refractive index to the choice of model. In fact, the $n_{eff}(\lambda)$ computed for the three different models at two different representative porosity levels (assuming realistic n for the oxide) shows that the two Bruggeman approaches yield almost indistinguishable results (Fig. 1). In contrast, the LLL model implies an $n_{eff}(\lambda)$ that is quite distinct from the Bruggeman behavior. Accordingly, analysis of porous films was carried out using only the S-BG and LLL models.

With the physical models established, the minimization was carried out by simply varying the fit parameters over a wide range of values and selecting those that yielded a minimum χ^2. The statistical uncertainty in the parameters, δx_j (where $\{x_j\}$ is the set of fit variables), was estimated by evaluating the expression,

$$\delta x_j = \left[\left(\frac{\partial T}{\partial x_j}\right)\Big|_{\{x_{i\neq j}\}}\right]^{-1} \delta T, \quad (11)$$

with δT being equivalent to the experimental uncertainty, estimated above as 0.01 from the noise level. All calculations were performed using in-house written MATLAB codes.

IV. OPTICAL PROPERTIES

A summary of the film-substrate systems prepared and examined in this work are provided in Table I. The first set of samples are three thick ($\sim$2 μm), dense films of two different compositions prepared by pulsed laser deposition and applied to two different types of substrates. With these films we determine the material properties to a high degree of

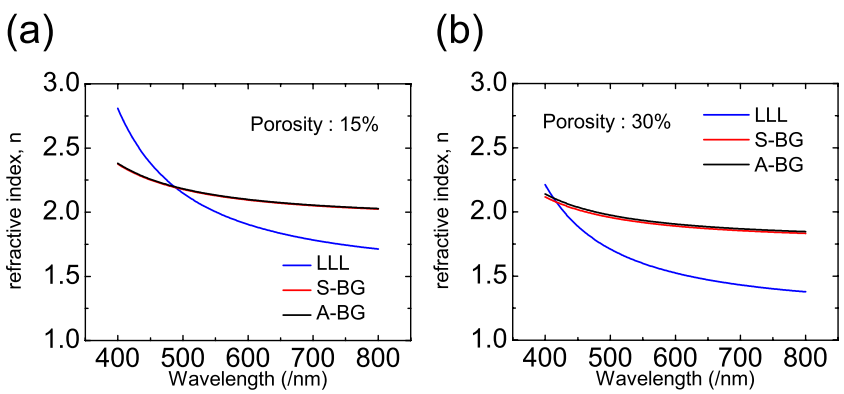

FIG. 1. Simulated dispersion behavior of refractive index (real part) for different effective medium models. (a) Assumed porosity: 15%, (b) assumed porosity: 30%. The two BG models are indistinguishable in terms of dispersion behavior.

TABLE I. Summary of general characteristics of ceria films prepared in this study.

Film #	Deposition method	Composition	Substrate	Thickness	Film density
1	PLD	Undoped	YSZ(100)	Thick[a]	Dense
2	PLD	20SDC	YSZ(100)	Thick[a]	Dense
3	PLD	Undoped	MgO(100)	Thick[a]	Dense
4	CVD	Undoped	YSZ(100)	Moderate[b]	Porous
5	PLD	20SDC	YSZ(100)	Moderate[b]	Porous
6	PLD	20SDC	YSZ(100)	Moderate[b]	Porous
7	CVD	Undoped	MgO(100)	Thin[c]	Porous
8	CVD	Undoped	YSZ(100)	Thin[c]	Dense

[a] ~2 μm.
[b] 500–1000 nm.
[c] <50 nm.

TABLE II. Dispersion relation fit parameters and indirect band gap energies obtained for dense PLD films on YSZ(100). Statistical errors (<0.1%) are too small to reflect the true uncertainty and values are simply reported to three significant digits.

Film	A (/nm^2)	B (unitless)	$E_g^{indirect}$ (/eV) Eq. (12)
#1, ceria	18200	0.272	3.23
#2, 20SDC	18600	0.287	3.15

accuracy, evaluate their variation with stoichiometry, and determine the influence, if any, of the substrate on the transmission analysis. The second set of samples constitute three thinner films (500–700 nm) grown under various conditions so as to yield microstructural differences. Analysis is carried out using fixed values of $n(\lambda)$ and $k(\lambda)$ obtained from the evaluation of the dense films. The final set of samples are a pair of extremely thin films for which the envelop method is entirely unsuitable. It is shown that, despite the absence of interference fringes, meaningful microstructural data can be obtained.

Figure 2 shows the SEM cross-sectional and AFM topological images of two dense ceria films (films 1 and 2, obtained by PLD) of differing stoichiometries grown on YSZ(100) with (SEM determined) thicknesses of 1820 and 1900 nm for dopant concentrations of 0 and 0.20, respectively. The films have negligible porosity and the rms roughnesses are, respectively, 2.5 and 2 nm. As described elsewhere, such PLD films adopt an epitaxial relationship with the YSZ substrate and are stoichiometrically identical to the target material.[2] The transmittance spectra obtained for these films are shown in Figure 3, along with the results of two fits. Because the films are thick and relatively smooth, the spectra show a large number of sharp interference fringes in the wavelength range of the measurement. Such films are amenable to treatment by a traditional envelope method just as they are to the full spectrum fitting undertaken in this work. Here, the inherent dispersion properties for the two compositions were determined by fixing rms roughness and film thickness at the independently, experimentally determined values just quoted, setting porosity to zero, and performing least squares fitting with only A and B as varied parameters. The resulting fits are shown in red in the plots in Figure 3 ("dispersion fit"), and the corresponding parameter values are provided in Table II.

The dispersion behavior implied for undoped and 20% Sm doped ceria is summarized in Figure 4, where Fig. 4(a) compares the present results for undoped ceria with literature values,[14–19] and Fig. 4(b) compares the three films studied here to one another. The index of refraction of undoped ceria obtained in this study is in general agreement with the many literature reports on this material. In all cases, the long-wavelength index falls between 2.1 and 2.4, and an upturn occurs around 400 nm as the photon energy approaches the average oscillator energy. As shown in Fig. 4(b), despite a difference in substrate, the results from the two undoped ceria films are almost identical, suggesting that artifacts arising from differences in substrate are negligible. The slightly lower index for CeO_2 on MgO (film 3) relative to that on

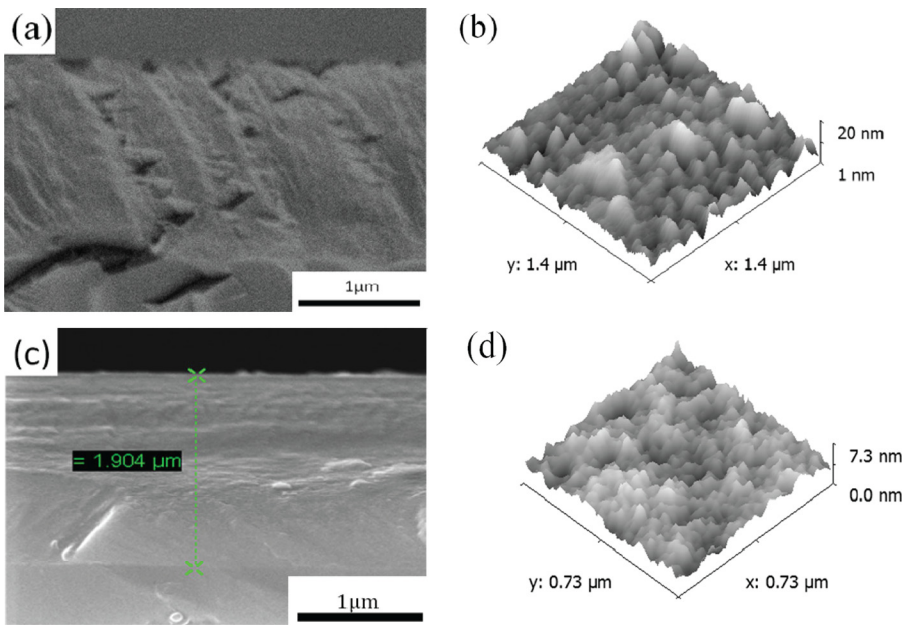

FIG. 2. Microstructural images of dense PLD films on YSZ (100): (a) SEM cross-sectional and (b) AFM topological images of undoped ceria (Film #1); and (c, d) analogous images for 20SDC (Film #2).

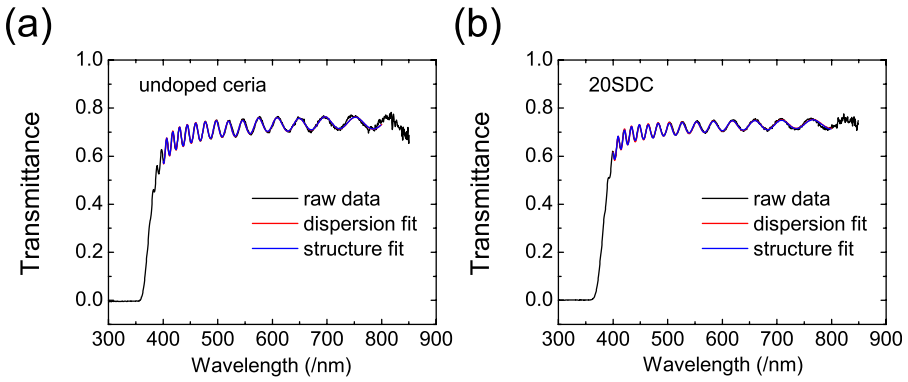

FIG. 3. Transmittance measurement and analysis for dense PLD films (a) undoped ceria (Film #1); (b) 20SDC (Film #2), of comparable thicknesses. Dispersion fits obtained upon varying A, B parameters in the Sellmeier dispersion relation, Eq. (3), with thickness and roughness fixed. Structure fits obtained upon varying porosity, thickness, and roughness, with known dispersion relationship from dispersion fits.

YSZ (film 1) may be due to lattice mismatch in the former case, which can, in turn, generate defects that lower material density. The index of refraction of the Sm-doped film is slightly lower still than either of the two doped films, but the impact of doping is small. Turning to the literature, only one prior study of the optical properties of Sm-doped ceria, which specifically focuses on the 15% Sm composition, could be found.[20] Those authors reported that the doped composition had a slightly higher index than the undoped (in contrast to the present work), but for both doped and undoped compositions the reported index was unusually low, below 2 over 400–800 nm. The low index of refraction suggests that porosity in the sol-gel derived films of that study, though not reported, was non-negligible, and thus trends with composition cannot be established from those results. The present study, comparing films 1 and 2 (both with 100% density), suggests a lowering of n by 0.03 at all wavelengths upon introduction of 20% Sm. Because Sm^{3+} ion has a higher dielectric polarizability than Ce^{4+}, an increase in n could be expected.[21] On the other hand, because the fluorite lattice expands upon doping, the opposite would be expected. The competition between these two characteristics prevents a straightforward prediction. The experimental results suggest the latter effect is slightly more significant.

The dispersion behavior can be interpreted in terms of the electronic properties of the solid. Specifically, the optical band gap, E_g, is related to the absorption coefficient (Eq. (1)) according to the expression,[14,19,23]

$$\alpha E_{ph} \propto (E_{ph} - E_g)^{\eta}, \tag{12}$$

where E_{ph} is the photon energy (given by $E_{ph} = hc/\lambda$, where h is Planck's constant and c is the speed of light) and η is a constant of value 0.5 for a direct transition and 2 for an indirect one. This expression was used here only for the determination of the indirect band gap (E_g^{indirect}), which is smaller than ~3.5 eV in ceria, because extinction coefficient values computed in the range below ~350 nm displayed too much scatter for analysis of the higher energy, direct band gap. An alternative method for interpretation of the dispersion behavior to obtain the direct band gap as suggested by Wemple and DiDomenico[22] was also found to be unsuitable. Thus, only the indirect band gap is reported, Table II.

V. MICROSTRUCTURAL PROPERTIES

A. Model validation using dense films

With the index of the ceria compositions well characterized, an initial validation of the fitting procedure was carried out using the data from the three dense films. The varied parameters were density, roughness, and film thickness. In this case, because both k and n are taken as known input parameters, there is no need to make use of the envelop method for any of the calculations, and only minimization of χ^2 in Eq. (4) was implemented. Table III summarizes the fitting results, and the computed T values for this case are shown in Figure 3 as the blue curves ("structure fit"). The parameters obtained from the fitting are in good agreement with the independently measured values, providing a validation of the procedures.

B. Properties of arbitrary typical films

Films 4–6 are representative of typical deposition conditions. Film 4 is a CVD-derived film of undoped ceria (growth temperature: 500 °C; deposition pressure: 1 Torr); films 5

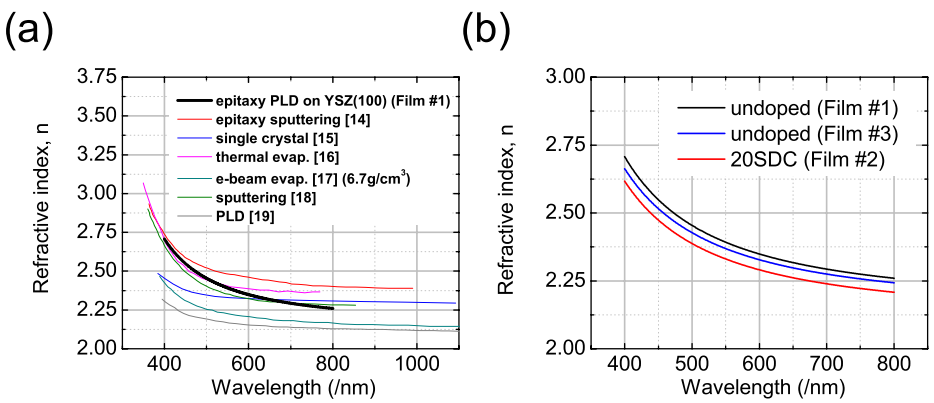

FIG. 4. Derived dispersion behavior of PLD grown films: (a) undoped ceria (Film #1) compared to literature results;[14–19] (b) substrate and dopant effects. Deposition on MgO(100) (Film #3) leads to a slight decrease in n relative to deposition on YSZ(100) (Film #1), likely due to poorer crystallographic registry between film and substrate creating a slightly lower density. Sm doping leads to a marginal decrease in n by 2%–3% over the wavelength range of interest, indicating minimal impact on the electronic characteristics.

TABLE III. Comparison between measured and fit microstructural parameters for dense, flat, thick ceria PLD films in Fig. 2, obtained using index of refraction values shown in Fig. 3. In all cases, fitted value of film porosity was below 0.01.

Film #	Composition	Thickness Fit/SEM (nm)	Film density Fit/set (relative)	rms roughness Fit/AFM (nm)	χ^2
1	Undoped	1822/1820	>0.99/1	4/2.5	210
2	20SDC	1900/1900	>0.99/1	5/2	112
3	Undoped	2300/2300	>0.99/1	10/13	762

and 6 are PLD-derived films of 20SDC deposited under 100 mTorr oxygen pressure, which, as already indicated, generates high porosity. The two PLD films differ only in terms of growth time (22 K and 30 K shots, respectively), leading to films of differing thickness. For all three analyses the $n(\lambda)$ and $k(\lambda)$ were taken from the results of the dense films and only microstructural parameters were varied. Because the films are less than 1 μm in thickness, as detailed below, only a limited number of interference fringes occur, Figures 5(a) and 6, and the fitting results were not particularly sensitive to film roughness (reflected in the sharpness of the fringes). Accordingly, only thickness and porosity were evaluated with roughness set to zero. Both the S-BG and LLL models for treating the porosity were considered. The limited number of fringes also implies that analysis by an envelope method alone would lead to high errors. Indeed, a comparative evaluation by the latter was found to severely underestimate the porosity (by 25% to 40%).

The fitting results for these three films are presented in Figures 5(a), 6(a), and 6(b), where the measured data are in black, the fits for the S-BG model are in blue, and the fits for the LLL model are in red. The results clearly demonstrate that the transmittance behavior is much better captured by the S-BG model. Though not shown, for completeness, the A-BG model was also explored and, not surprisingly, the result was barely distinguishable from the S-BG model for all three films. The extracted microstructural parameters are summarized in Table IV. For all three films the χ^2 values, also provided in the table, are significantly smaller for the S-BG model than the LLL model, consistent with the visual differences evident in the relevant figures indicating that the former provides a better representation of the film microstructures. In the case of Film 4, for which XRR analysis was performed, the porosity value of 0.40 ± 0.13 determined from the S-BG fit matches quite well to the XRR value of 0.4, and is closer to this XRR porosity than the LLL model value of 0.367 ± 0.001. Similarly, in the case of Film 6, for which SEM imaging was performed, the thickness value of 717 ± 29 nm determined from the S-BG fit matches quite well to the directly measured value of 740 nm, and is closer than the value of 649 ± 33 determined from the LLL model. The computed thickness of Film 5 using the S-BG model is 532 ± 67, almost precisely consistent with the 35% shorter growth time for this film relative to Film 6. Although roughness was not evaluated from the transmittance data, it is noteworthy that the XRR measurement yielded a root-mean-square roughness of 12 nm for Film 4 (Figure 5(b)), comparable to the value of 10 nm obtained from an AFM measurement of this same film.

While a detailed discussion of film growth characteristics is beyond the scope this work, the two porous PLD-grown films [20SDC on YSZ(100)] reveal interesting

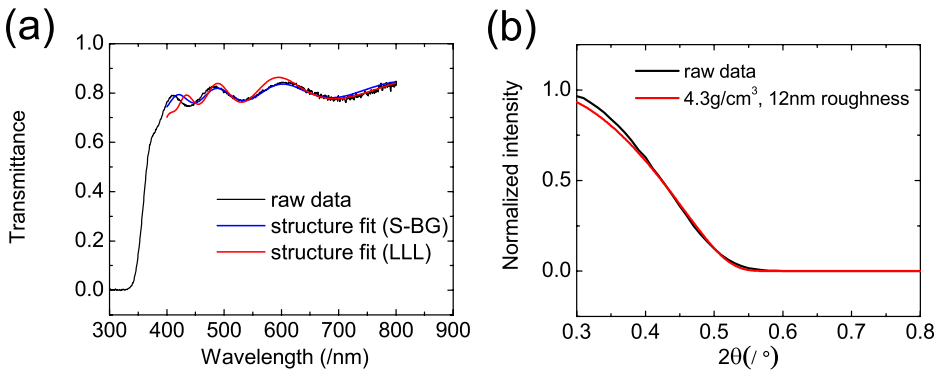

FIG. 5. Properties of porous, undoped ceria deposited on YSZ(100) by CVD (Film #4): (a) Measured and modeled transmittance spectra, where fits were performed by varying microstructural parameters within the framework of the S-BG and LLL effective medium models and (b) measured and simulated reflectometry curves, where the simulation was performed for a film of manually optimized porosity of 40% (4.3 g/cm^3 is 60% of the theoretical density of 7.22 g/cm^3) and rms roughness of 12 nm.

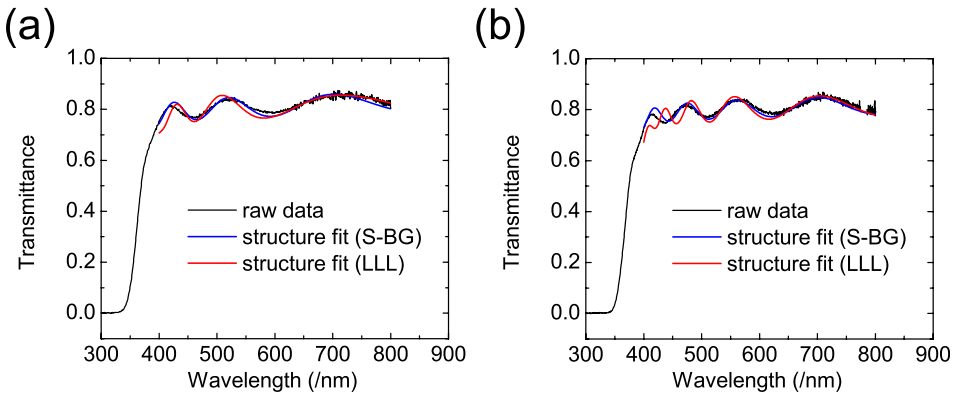

FIG. 6. Transmittance measurement and analysis for porous PLD films of undoped ceria of differing thicknesses: (a) 22 K shots (Film #5) and (b) 30 K shots (Film #6). Fits were performed by varying microstructural parameters within the framework of the S-BG and LLL effective medium models.

TABLE IV. Summary of microstructural fit parameters obtained from transmittance spectra analysis of Films 4-6. Results obtained from S-BG and LLL effective medium theories are compared, and where available, these are also compared to independent structural measurements.

Film #	Method	Thickness(/nm)	Porosity	χ^2
	S-BG	589 ± 63	0.40 ± 0.13	672
4[a]	LLL	507 ± 36	0.367 ± 0.001	1964
	XRR	…	0.4	…
5	S-BG	532 ± 69	0.45 ± 0.07	687
	LLL	420 ± 41	0.364 ± 0.001	1610
	S-BG	717 ± 29	0.40 ± 0.09	669
6	LLL	649 ± 33	0.333 ± 0.001	2270
	SEM	740 ± 30	…	…

[a]rms roughness by AFM = 10 nm, by XRR = 12 nm.

behavior. Despite the identical growth conditions, the computed porosities differ, determined as 0.45 and 0.40, respectively, for Films 5 and 6. This result is taken to represent the actual film growth characteristics. It has been observed that with increasing film thickness, the individual columns of the columnar structure increase in diameter, whereas the number density of columns decreases.[24] This overall coarsening of the structure apparently causes an increase in overall film density with increasing film thickness. Although the model for transmittance employed here does not account for graded porosity, the variation observed here, just 10% over a thickness corresponding to 35% of the total, is sufficiently small that it does not have significant impact, for example, on the accuracy of the derived film thickness.

C. Properties of very thin films (<50 nm)

Films 7 and 8 (Table I) are very thin samples representing the initial conditions of CVD film growth. The deposition was carried out for only ~10 s on two different substrates: MgO(100) and YSZ(100). These films were grown simultaneously in a single deposition run (growth temperature: 450 °C; deposition pressure: 3 Torr) so as to insure a meaningful interpretation of substrate influence. Given the good lattice match between ceria and YSZ, whereas that between ceria and MgO is poor, one can anticipate a difference in growth characteristics, particularly at the initial stages. The spectra, Figure 7, are almost featureless as a result of the extreme thinness of the films, entirely precluding an analysis by the envelope method. Using the full spectrum fitting approach and the S-BG model for porosity, we extract film thickness and porosity for both samples as reported in Table V. The raw data are shown in black and the fits in red. As with the earlier films, the data are well-represented. The porosity in the case of deposition on MgO is 0.4, whereas on YSZ it is negligible. As a measure of the sensitivity of the numerical procedures, simulated spectra assuming a porosity of 0.2 are shown (blue curves) on both plots. The simulation confirms that a porosity of 0.2 underestimates the transmittance through the more porous film on MgO and overestimates that through the denser film on YSZ.

TABLE V. Summary of fitting results from Films #7 and #8. Larger χ^2 for Film #8 is mainly from the higher level of noise in the spectrum (Fig. 7).

Film #	Substrate	Thickness (/nm)	Porosity	χ^2
7	MgO(100)	30 ± 80	0.40 ± 0.10	184
8	YSZ(100)	14 ± 10	0.00 ± 0.21	415

The XRR measurement of Film 8, carried out to validate the transmittance analysis, is in good agreement with the conclusions drawn for this film. In Figure 8 the measured XRR data are compared to simulations in which (a) the film thickness is varied and (b) the film density is varied, assuming zero roughness in both cases. In a very general sense, the frequency of the oscillations in the XRR spectrum reflects the film thickness and the sharpness and position of the first drop-off reflect a convolution of roughness and density. While a precise determination of the physical parameters from these data (which involves modeling comparable to that carried out for the transmittance analysis) is beyond the scope of the present work, one can, nonetheless, conclude the spectrum is consistent with a film that is 10-20 nm in thickness (based on the simulations in which thickness is varied) and has a density of approximately 85% (based on the simulations in which density is varied). These values compare well with the thickness and density values, 14 ± 10 nm and 100 ± 21%, respectively, obtained from the analysis of the optical transmittance data.

The above results demonstrate that the substrate indeed has a profound influence on film growth characteristics. The

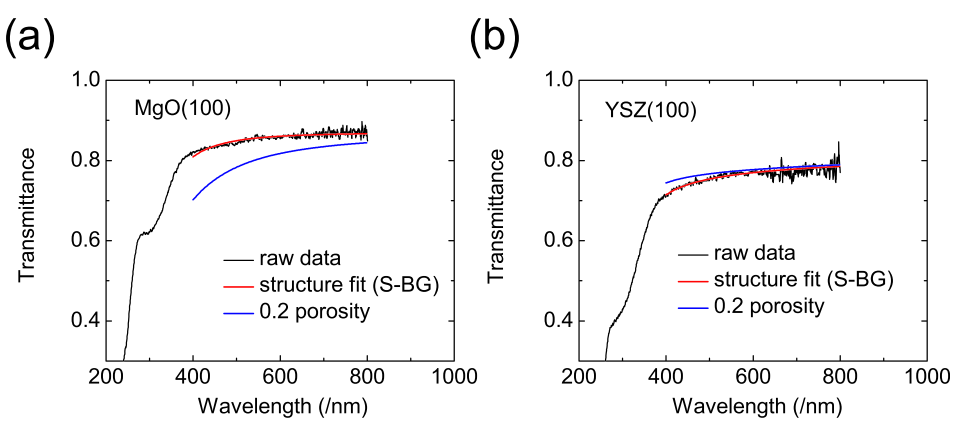

FIG. 7. Transmittance measurement and analysis for ultra-thin CVD films of undoped ceria on differing substrates: (a) on MgO(100) (Film #7) and (b) on YSZ(100) (Film #8). Fits were performed by varying microstructural parameters within the framework of the S-BG, varying thickness and porosity (red lines). Blue lines are simulated transmittance curves, generated assuming 0.2 porosity and the thickness as obtained from the initial respective fits.

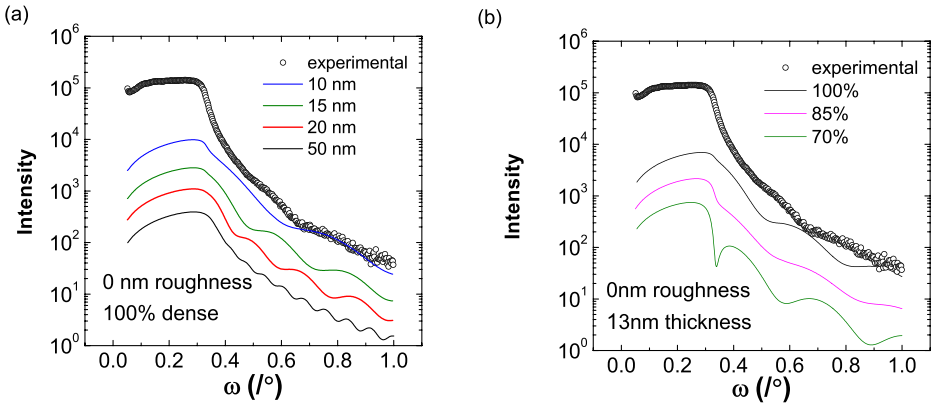

FIG. 8. XRR trace for a film comparable to Film #8 (same deposition condition). Experimental data compared to simulations with parameters as given on the plots. Simulated curves are from (a) thickness variation, (b) density variation.

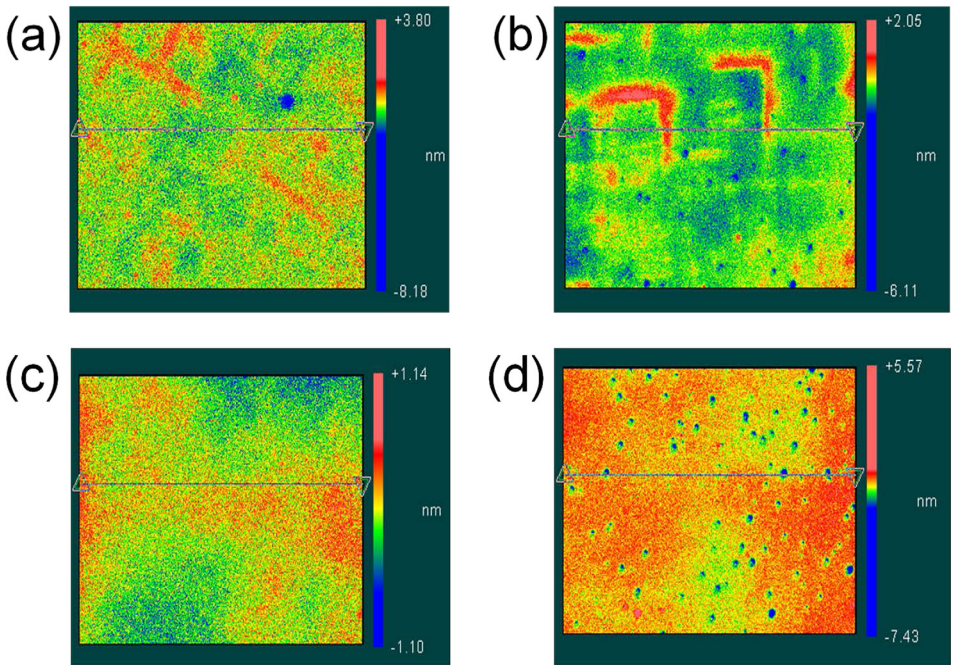

FIG. 9. Surface topography maps. MgO(100) substrate: (a) before deposition, (b) after deposition. YSZ(100) substrate: (c) before deposition, (d) after deposition.

SWLI measurements for as-purchased and post-deposition MgO and YSZ substrates, Figure 9, point to the origin of these differences. Analysis of the images of the films shows the root-mean-square roughness in *all* cases to be <0.5 nm. However, the MgO(100) substrate has clear surface striations that intersect at 90° angles and presumably follow crystallographic planes, whereas the YZS(100) substrate has a homogenous surface topology. The sharp features of the as-purchased MgO(100) surface are replicated and even accentuated in the ceria film grown on this substrate, with film deposition occurring preferentially in the vicinity of the striations. In contrast, the ceria on YSZ has a relatively homogeneous thickness, with the exception of small pits distributed throughout the film. These differences lead to the differences in density detected by the transmittance analysis. The substrate influence is further reflected in the X-ray rocking curve measurements taken about the ceria 200 peak, Figure 10. Here, a sharp peak is observed only when the substrate is YSZ, indicating that the sharp geometric features of the MgO substrate are not conducive to oriented growth of the ceria film.

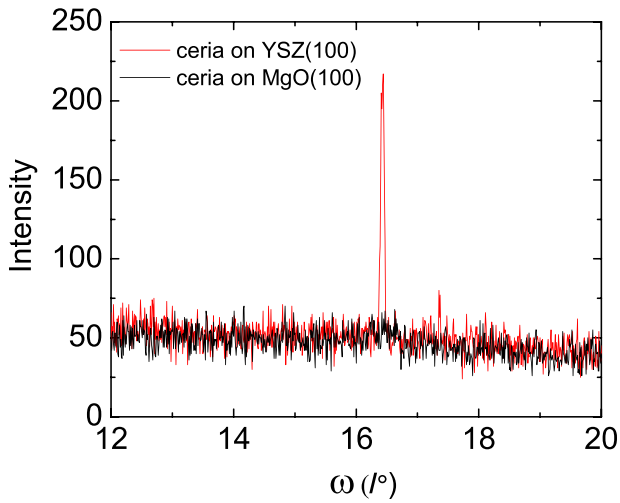

FIG. 10. X-ray rocking curves (ω scan) about the ceria 200 peak for two different films with ultra-thin ceria grown by CVD (Films #7 and #8). The ceria on YSZ(100) shows a sharp peak, indicating an epitaxial relationship at the initial stages of film growth, whereas that grown on MgO does not. The FWHM of the peak is found to be 0.066° by Gaussian fitting.

VI. SUMMARY AND CONCLUSION

An optical transmittance analysis procedure was developed to extract the complex refractive index ***n***, film thickness, and porosity of a film grown on a substrate with known index and zero extinction. Using thick, dense, smooth films, the dispersion behavior of undoped and 20% Sm doped ceria was measured. The optical properties of the two compositions are similar, reflecting similarity in the electronic bonding characteristics. The indirect band gap implied by these data, ~3.2 eV, falls within the range of values reported in the literature.

For films with known dispersion behavior but unknown microstructural characteristics, the latter (film thickness, porosity, and roughness) could be accurately extracted from the analysis methodology, as confirmed by comparison with SEM, profilometry, AFM, and XRR measurements. It was further found that the symmetric Bruggeman model for material microstructure best represents the optical transmittance data over the alternative LLL model. The results of the analysis demonstrate the value of the transmittance method for evaluating film growth characteristics. Even for films as thin as 14 nm which display no interference fringes in their transmittance spectra, thickness and porosity can be determined. While, in principle, XRR could be used to evaluate such films, optical transmittance has the advantage of fast measurements and ease of data acquisitions. In addition, unlike XRR, even very small area samples can be evaluated. Indeed, one can envision confining the illumination area to perform 2-D mapping of the transmittance. Such an approach has recently been demonstrated to obtain thickness maps for relatively thick films (>5 μm) with presumably well-defined interference fringes.[25]

ACKNOWLEDGMENTS

The authors gratefully acknowledge financial support from the National Science Foundation under award CBET-038307. Additional support was provided by the Global Climate and Environment Program administered by Stanford University. Professor George Rossman kindly provided access to optical equipment and Professor Harry Atwater to XRR instrumentation in their respective laboratories. This work furthermore made use of facilities operated by the Geological and Planetary Sciences Division and by the Kavli Nanoscience Institute at Caltech.

[1]R. Swanepoel, J. Phys. E: Sci. Instrum. **16**, 1214 (1983).
[2]W. C. Chueh, Y. Hao, W. Jung, and S. M. Haile, Nature Mater. **11**, 155 (2012).
[3]M. Kubinyi, N. Benkö, A. Grofcsik, and W. Jeremy Jones, Thin Solid Films **286**, 164 (1996).
[4]N. Maley, Phys. Rev. B. **46**, 2078 (1992).
[5]S. R. Bhattacharyya, R. N. Gayen, R. Paul, and A. K. Pal, Thin Solid Films **517**, 5530 (2009).
[6]R. D. Shannon, R. C. Shannon, O. Medenbach, and R. X. Fischer, J. Phys. Chem. Ref. Data. **31**, 931 (2002).
[7]R. Swanepoel, J. Phys. E: Sci. Instrum. **17**, 896 (1984).
[8]V. Lucarini, J. J. Saarinen, K.-E. Peiponen, and E. M. Vartiainen, *Kramers–Kronig Relations in Optical Materials Research* (Springer, 2005).
[9]W. M. Merrill, R. E. Diaz, M. M. LoRe, M. C. Squires, and N. G. Alexopoulos, IEEE Trans. Antennas Propag. **47**, 142 (1999).
[10]E. Barsoukov and J. R. Macdonald, *Impedance Spectroscopy: Theory, Experiment, and Applications* (Wiley, 2005), p. 221.
[11]H. Looyenga, Physica **31**, 401 (1965).
[12]L. D. Landau and E. M. Lifshitz, *Electrodynamcis of Continuous Media* (Pergamon, 1984).
[13]S. O. Nelson and T. -S You, J. Phys. D: Appl. Phys. **23**, 346 (1990).
[14]S. Guo, H. Arwin, S. N. Jacobsen, K. Järrendahl, and U. Helmersson, J. Appl. Phys. **77**, 5369 (1995).
[15]F. Marabelli and P. Wachter, Phys. Rev. B. **36**, 1238 (1987).
[16]G. Hass, J. B. Ramsey, and R. Thun, J. Opt. Soc. Am. **48**, 324 (1958).
[17]P. Patsalas, S. Logothetidis, and C. Metaxa, Appl. Phys. Lett. **81**, 466 (2002).
[18]R. M. Bueno, J. M. Martinez-Duart, M. Hernandez-Velez, and L. Vasquez, J. Mater. Sci. **32**, 1861 (1997).
[19]L. Méchin, A. Chabli, F. Bertin, M. Burdin, G. Rolland, C. Vannuffel, and J.-C. Villégier, J. Appl. Phys. **84**, 4935 (1998).
[20]A. Hartridge, M. G. Krishna, and A. K. Bhattacharya, J. Phys. Chem. Solids **59**, 859 (1998).
[21]R. D. Shannon, J. Appl. Phys. **73**, 348 (1993).
[22]S. H. Wemple and M. DiDomenico, Phys. Rev. B **3**, 1338 (1971).
[23]P. Patsalas, S. Logothetidis, L. Sygellou and S. Kennou, Phys. Rev. B. **68**, 35104 (2003).
[24]N. Pryds, K. Rodrigo, S. Linderoth, and J. Schou, Appl. Surf. Sci. **255**(10), 5232 (2009).
[25]Y. Chang, G. Badano, E. Jiang, J. W. Garland, J. Zhao, C. H. Grein, and S. Sivananthan, J. Cryst. Growth **277**, 78 (2005).